Astron. Astrophys. 321, 111–122 (1997)

ASTRONOMY AND ASTROPHYSICS

The fundamental plane of early-type galaxies: non-homology of the spatial structure⋆

Ph. Prugniel and F. Simien

CRAL-Observatoire de Lyon (CNRS: UMR 142), F-69561 St-Genis-Laval Cedex, France

Received 26 April 1996 / Accepted 12 September 1996

Abstract. Parametrizing their light distribution with a Sérsic profile, we show that the non-homology in the structure of early-type galaxies has a measurable incidence on their scaling relations. Indeed, the Sérsic exponent (i.e., the shape of the photometric profile) correlates with the residuals to the Fundamental Plane. This correlation is in excellent agreement with the theoretical expectation for isotropic galaxies.

Adding together the contributions of: (i) the stellar population, (ii) the rotational support, and (iii) the non-homology, fully accounts for the tilt of the Fundamental Plane. This supports the hypothesis of a constant stellar to dynamical mass ratio in the luminous region of early-type galaxies.

We confirm the existence of relations between the Sérsic exponent, n, and the effective radius or the absolute magnitude, and we give indications for a saturation of this index for the bright ($M_B < -20$) or large ($r_e > 6.3$ kpc) galaxies at a value compatible with the de Vaucouleurs law ($n = 4$).

Key words: galaxies: elliptical & lenticular, cD – galaxies: fundamental parameters – galaxies: general – galaxies: photometry – galaxies: kinematics and dynamics

1. Introduction

The goal of this paper is to study the effect of the non-homology of the spatial structure of early-type galaxies on their scaling relations, and, in particular, on the tilt of the Fundamental Plane (FP).

The FP of early-type galaxies (Dressler et al. 1987; Djorgovski & Davies 1987) expresses the quasi-linearity of their scaling relations. In other words, the scales of the kinetic and gravitational energies (T and W) and that of the mass ($\mathscr{M}$), linked by the virial theorem, are given by the central velocity dispersion (σ_0), the effective radius (r_e) and the luminosity (L). The equilibrium relation writes:

$$k_K \sigma_0^2 = (2\pi)^{-1} k_S (\mathscr{M}/L)\, L\, r_e^{-1}, \tag{1a}$$

or

$$k_K \sigma_0^2 = k_S (\mathscr{M}/L)\, L^{1/2}\, I_e^{1/2}, \tag{1b}$$

when introducing I_e, the mean surface brightness within the effective circular aperture. Other definitions of the fiducial radius and velocity dispersion could equivalently be choosen. The factors k_K, k_S and $\mathscr{M}/L$ are respectively the kinematical, gravitational and mass scaling parameters (Prugniel & Simien 1996: hereafter PS96):

$$T/\mathscr{M} = k_K \sigma_0^2, \tag{2}$$

$$W/\mathscr{M} = k_S \mathscr{M}/r_e, \tag{3}$$

$$\mathscr{M} = (\mathscr{M}/L)\, L. \tag{4}$$

In PS96 we separated the mass-to-light ratio into: $\mathscr{M}/L = (\mathscr{M}/\mathscr{M}_*)\,(\mathscr{M}_*/L)$, introducing $\mathscr{M}_*/\mathscr{M}$, the dynamical-to-stellar mass ratio.

1.1. non-linearity of the scaling relations

If the scaling relations were linear, k_K, k_S and $\mathscr{M}/L$ would be constant factors. Actually, the FP analysis establishes that:

$$k_S\, k_K^{-1}\, \mathscr{M}/L = L^{\beta}, \tag{5}$$

with $\beta \approx 0.2$ when the photometric data are in the B band; β is known as the *tilt* of the FP.

Detailed analyses reveal the secondary importance of other parameters in the scaling relations. The most apparent one comes from the characteristics of the stellar population (mean age and mean metallicity). Gregg (1992) has shown that metal-weak galaxies systematically depart from the FP in the same direction, resulting in the determination of biased peculiar velocities. Guzmán & Lucey (1993) explain a systematic difference in the residuals of the $D_n - \sigma$ relations between the core and halo of the Coma cluster as apparently related to the mean metallicity of the galaxies. Several other papers have incorporated metallicity parameters to the scaling relations (e.g., Guzmán et al. 1993;

Send offprint requests to: F. Simien (simien@obs.univ-lyon1.fr)

⋆ Based in part on observations collected at the Observatoire de Haute-Provence.

Jørgensen et al. 1993; van Albada et al. 1995). In PS96 we have generalized these results, showing that the residuals of the FP do correlate with some characteristics of the stellar population, namely the broad-band colors and the Mg_2 index. We presented evidence for this effect contributing for $\beta_* \approx 0.10$ to the total value of β in the B band.

A second effect is the contribution of the rotation to the total kinetic energy (Prugniel & Simien 1994: hereafter PS94; Bender et al. 1994; D'Onofrio et al. 1995; Prugniel & Simien 1995). In PS96 we show that the rotational support accounts for $\beta_R \approx 0.06$ to β.

The third effect which has been addressed in the literature is that of the spatial non-homology. Hjorth & Madsen (1995) show that the deviations from the $r^{1/4}$ profile could account for the tilt of the FP, and Bender et al. (1992) argue that the differences in the radial distribution of the mass cannot explain the contrast in the apparent $\mathscr{M}/L$ between elliptical and dwarf spheroidal galaxies. The present paper gives a quantitative analysis of this effect.

Other effects may also play a non-negligible role; let us mention two of them: a) the intrinsic flattening (Saglia et al. 1993) and the degree of triaxiality, and b) the presence of hidden stars (i.e., low-luminosity stars or stellar remnants) which are not apparent from the colors or line-strength indices (Zepf & Silk 1996).

1.2. Coupling between the scaling relations

Strictly speaking, there is no reason to assume that the three scaling relations are independent. But, for the sake of simplicity, we will suppose that $\mathscr{M}/\mathscr{L}$ does not depend on k_S and k_K. This will allow us to separate the stellar-population effect ($\mathscr{M}_*/\mathscr{L} \propto \mathscr{L}^{\beta_*}$) which, as indicated above, is a major contributor to the tilt.

In contrast, we will consider the coupling of the two other scaling relations: k_K and k_S, because the spatial density and velocity distributions are linked by the equations of the stellar hydrodynamics.

This coupling is already present in the effect of the rotational support: a rotating galaxy flattens and its gravitational energy changes; but we neglected this effect, in PS94, because it is smeared by the projection onto the plane of the sky.

In the present paper, we are interested in the non-homology of the spatial structure and it is not possible to presuppose if the effect will rather affect k_S or k_K. We are thus led to re-formulate the scaling relations as follows:

$$k_S k_K^{-1} = l_R l_S l_o, \tag{6}$$

where l_R and l_S are, respectively, the observed contributions of the rotation and of the structure non-homology. The factor l_o embeds the other observational contributions (e.g., that linked to the intrinsic flattening or triaxiallity) and will not be studied here. The parametrization of the light distribution by a Sérsic profile will constrain l_S, and physical considerations (in practice the assumption of isotropy) will give a prediction of the contributions to k_K and k_S.

1.3. Outline of the paper

In Sect. 2, we present the sample and the data used in this paper, and we describe the fitting of Sérsic growth-curves to the aperture photometry data. In Sect. 3, we derive the standard solution of the FP, including the contribution of the stellar population. In Sect. 4, we analyse the monovariate correlations involving the Sérsic exponent and its correlation with the residuals from the FP. In Sect. 5, we compare the observed result to the theoretical expectation for a Sérsic profile. And a discussion is presented in Sect. 6.

2. Sample and data

2.1. Sample

We have extended the sample described in PS96 by adding galaxies obeying the same selection criteria, and for which the necessary data have become available from recent publications, in particular from Prugniel & Simien (in preparation).

The photometric data used in this paper are described below. The kinematic data, i.e., the central velocity dispersion and the maximum velocity of rotation, were taken from the updated verion of the catalogues described in PS96 (this updated version is available on the WWW at the following URL: http://obs.univ-lyon1.fr/~prugniel/home_galaxies.html). The Mg_2 indices are averages of the different published values; the main sources are: Davies et al. (1987), Dressler et al. (1991), Jørgensen et al. (1995) (the detailed compilation may be obtained on request).

The distances and different corrections on the photometry and diameters are defined as in PS96. The Galactic absorptions are from Burstein & Heiles (1982) and the distances are computed from the model of Faber & Burstein (1988), which includes Virgocentric and Great-Attractor terms. We scaled the distances to $H_0 = 75\,\mathrm{km\,s^{-1}Mpc^{-1}}$, corresponding to a distance modulus of 31.02 for the Virgo cluster. For the Local-Group galaxies (NGC 147, 185, 205, 221, and the dwarf spheroidals), we adopted the distances from van den Bergh (1989).

As in PS96, the global sample has been divided into subsamples with common characteristics, as follows:

1) *bona fide* ellipticals: 323 objects;

2) Compact ellipticals (CEs): NGC 221, NGC 4486B and NGC5846A;

3) Diffuse ellipticals (also called dwarfs, dEs), and low-luminosity ellipticals (LLEs): 38 objects, mostly M31's companions and galaxies in Virgo.

4) Peculiar ellipticals, dusty objects, interacting and supposed merger remnants: 61 objects;

5) Lenticular galaxies (types S0, SB0, and Sa): 201 objects;

6) Dwarf spheroidal galaxies (dSphs): seven objects, Carina, Draco, Fornax, Sculptor, Leo1, Leo2 and Ursa Minor.

2.2. The photometric parameters

The photometric parameters were derived from growth-curve fitting using aperture-photometry data. This method has been the basis for the determination of the magnitudes and surface

brightnesses in the RC3 (de Vaucouleurs et al. 1991; Buta et al. 1995). In the present case, we have extended the database of photoelectric photometry by CCD photometry, taken in the literature and from an ongoing long-term programme conducted at the 1.2 meter telescope of the Observatoire de Haute-Provence. This is a crucial point of our study: the very high internal precision of the CCD photometry, allied to the better absolute precision of the photoelectric photometry, provides both a good constraint on the shape of the growth curve, and an accurate value of the zero point. In general, the authors of CCD surface photometry do not provide the integrated magnitudes through circular apertures, and we had to simulate this integration on reconstructed images issued from the published photometric and geometric profiles. Our photometric database will be published in Prugniel & Héreaudau (in preparation).

Following Caon et al. (1993 = CCO93), we adopt the Sérsic (1968) law for the description of the photometric profile:

$$\mu_{[\mathrm{mag\ arcsec}^{-2}]} = \zeta \left(\frac{r}{r_e}\right)^{1/n} + \xi + M, \qquad (7)$$

where μ is the local surface brightness at radius r, r_e is the effective radius and M the total magnitude. ζ and ξ are constants scaling the size and the luminosity. The Sérsic law describes both the exponential profile ($n = 1$) characteristic of diffuse ellipticals (dEs), and the de Vaucouleurs profile ($n = 4$) suited to ellipticals. The corresponding curves of growth are derived in Appendix A.

The colors used in this paper result from linear interpolations (or in some cases extrapolations) at the effective radius using the color index vs. $\log(r)$ relations.

For galaxies with more than 10 photometric apertures available, we fitted a Sérsic law; otherwise we fitted a de Vaucouleurs law, and the object was subsequently excluded from correlations involving the value of n. The fitting code returns the total magnitude, the mean surface brightness within the effective circular aperture, the Sérsic exponent, and the corresponding estimated errors. We defined a photometric quality Q, based on the magnitude of the errors and on the number of available apertures. The class Q=6 is reserved to those galaxies not directly calibrated in the B-band, their B-magnitude is derived assuming standard color indices (this is our worse class). Q=5 is given to the galaxies whose magnitude determination required an extrapolation larger than 0.5 magnitude, and Q=4 to the galaxies having less than 10 apertures measured. The three better classes gather the galaxies that could be fitted to a Sérsic law sorted according to the errors on the photometry: Q=1 is given to the 20% with the smallest errors, Q=3 to the 20% worse, and Q=2 to the rest.

The resulting magnitudes and surface brightness compares with the values of the RC3 as: B_T(PS) $-$ $\mathrm{B_T}$(RC3) = -0.04 with a rms scatter of 0.17, and μ_e(PS) $-$ μ_e(RC3) = 0.06 with a rms scatter of 0.43. We also stress that these errors are strongly correlated: $\delta(B_T) = -0.4\delta(\mu_e)$. This error correlation has been described in other places, eg. Burstein et al. (1987) and Hamabe & Kormendy (1987).

Our values of the Sérsic exponent, compared with those of CCO93 and D'Onofrio et al. (1994), show a good agreement for $n < 5$, but, while CCO93 find large n, up to $n = 15$, our values never exceed ≈ 6. The details of this comparison will be discussed in D'Onofrio & Prugniel (1996).

3. Standard equation of the Fundamental Plane

As in PS96, we start from the following definition of the FP:

$$R = 2\log(\sigma_0) + 0.2(1+2\beta)M_B + 0.2\mu_e + \eta, \qquad (8)$$

where R defines the residuals with respect to the plane along the $\log(\sigma_0)$ axis, σ_0 is the central velocity dispersion, M_B is the absolute blue magnitude, μ_e is the effective surface brightness, and β is a free parameter, often referred to as the *tilt* of the FP; η is a zero-point constant.

The mono- or bivariate nature of this relation has been discussed in PS96. We have adopted this form, rather than the more general bivariate equation involving an independent free coefficient γ before μ_e, because of the strong coupling between β and γ. This coupling results from the correlation between B_T and μ_e.

The only difference with the fitting method adopted in PS96 is that we presently take into account the observational errors in order to assign an individual weight to each galaxy. Table 1 presents the results of the fit. The coefficients are very similar to those adopted in PS96.

We are now going to compute a solution including the effect of the stellar population, since this has been shown to be a major contribution to the tilt of the FP. To do that, we first define an indicator of the *quality* of the stellar population by combining the colors and the $\mathrm{Mg_2}$ index.

3.1. Combined stellar-population indicator

In PS96, we have found that the residuals R from the FP do correlate with the broad-band colors and $\mathrm{Mg_2}$ index. We interpreted it as an age and/or metallicity effect, and we have shown that it contributes to roughly half the tilt of the FP. Using these relations in the present paper would imply the handling of five relations in parallel (the four broad-band colors and $\mathrm{Mg_2}$), representing a single effect.

As a simplification, we will instead combine these relations by defining a relevant, single stellar-population indicator P. We first choose $B - V$ as the reference for normalizing the other indices:

$$C_i = a_i(B-V) + b_i. \qquad (9)$$

In this relation, i runs for all the colors and for $\mathrm{Mg_2}$; C is any one of the indices, and a and b are normalization constants whose values, fitted to the whole sample, are listed in Table 2. Inverting this relation gives the normalized indices:

$$D_i = a_i^{-1}(C_i - b_i). \qquad (10)$$

Then, P is defined as a weighted mean of the available D_i indices. The weights (w_i) are chosen to reflect the sensitivity of each index to the *quality* of the stellar population: they are taken

Table 1. Fit of the Fundamental Plane

Sample	$N^{(1)}$	β	η	$u^{(2)}$	$\delta^{(2)}$	$v^{(2)}$	rms$^{(3)}$
PS96	231	0.22 ± 0.02	-3.10 ± 0.17	0.0	0.0	0.00	0.132
Ellipticals	263	0.21 ± 0.02	-3.12 ± 0.16	0.0	0.0	0.00	0.128
Whole sample	465	0.18 ± 0.02	-3.41 ± 0.13	0.0	0.0	0.00	0.158
Ellipticals	245	0.11 ± 0.02	-3.89 ± 0.14	3.0	0.0	0.00	0.113
Whole sample	432	0.11 ± 0.01	-3.91 ± 0.12	3.0	0.0	0.00	0.135
Ellipticals	143	0.15 ± 0.03	-3.67 ± 0.23	0.0	1.0	0.00	0.137
Whole sample	259	0.09 ± 0.02	-4.14 ± 0.17	0.0	1.0	0.00	0.158
Ellipticals	139	0.06 ± 0.03	-4.32 ± 0.21	3.0	1.0	0.00	0.121
Whole sample	256	0.04 ± 0.02	-4.56 ± 0.16	3.0	1.0	0.00	0.142
Ellipticals	246	0.19 ± 0.02	-3.19 ± 0.15	0.0	0.0	0.04	0.118
Whole sample	405	0.16 ± 0.02	-3.39 ± 0.14	0.0	0.0	0.04	0.149
Ellipticals	230	0.08 ± 0.02	-4.01 ± 0.14	3.0	0.0	0.04	0.106
Whole sample	381	0.08 ± 0.01	-3.95 ± 0.12	3.0	0.0	0.04	0.126
Ellipticals	134	-0.01 ± 0.03	-4.17 ± 0.19	3.0	1.0	0.04	0.107
Whole sample	231	0.03 ± 0.02	-4.47 ± 0.15	3.0	1.0	0.04	0.123

Notes: The sample: "*Ellipticals*" corresponds to the first subsample defined in Sect. 2.1; β, η, u, δ and v are defined in Eqs. (8), (13) & (15). The residual dispersion (rms) is measured along the $\log(\sigma_0)$ axis. (1) Number of galaxies used for the fit after 2.5σ clipping. It also depends on which of u, δ and v are forced to 0 (see below). (2) Forced value. When the value is 0 the galaxies for which the associated measurement is not available are included in the fit; this is particularly significant in the case of δ, because $V_{\rm max}$ is available for only about half the objects. (3) Root mean square residual from the fit, expressed in the units of $\log(\sigma_0^2)$.

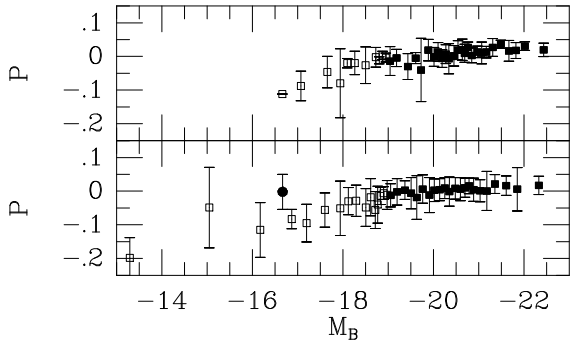

Fig. 1. The stellar-population indicator (P) vs. the absolute B magnitude (M_B). Upper panel: Bona fide ellipticals. *filled squares*: bins of 10 galaxies; *open square*: bins of 4 galaxies. Lower panel: Whole sample. *filled squares*: bins of 20 galaxies; *open square*: bins of 8 galaxies. *filled circle*: Compact elliptical galaxies (3 objects). The error bars correspond to the rms dispersion within each box

Table 2. Normalization coefficients for the stellar-population indices

Elliptical galaxies				
Index	$N^{(1)}$	a_i	b_i	w_i
U-B	238	1.10 ± 0.10	-0.52 ± 0.09	0.71
V-R	223	0.18 ± 0.07	0.41 ± 0.07	0.70
V-I	165	0.95 ± 0.09	0.30 ± 0.09	1.04
Mg_2	212	0.293 ± 0.042	0.026 ± 0.040	0.93
Whole sample				
Index	$N^{(1)}$	a_i	b_i	w_i
U-B	444	1.23 ± 0.05	-0.65 ± 0.05	0.69
V-R	394	0.37 ± 0.03	0.23 ± 0.03	0.62
V-I	310	0.90 ± 0.05	0.36 ± 0.04	1.11
Mg_2	291	0.387 ± 0.033	-0.066 ± 0.031	0.91

Note: (1) Size of the sample

as the square of the inverse of the relative error on the slope of the R vs. C_i relations derived in PS96 (normalized to $w_{B-V} = 1$). Fig. 1 shows the trend of P with respect to luminosity.

In this process, we are clearly overlooking the fact that the *quality* of the stellar population has to be represented by more than one parameter. At least the mean age and the mean metallicity are needed and, more realistically, the actual distribution of ages and metallicity should be considered. However, all our indices are almost as sensitive to both age and metallicity, and they could hardly be used to desantangle these effects. We neither make the most of the fact that the colors and the Mg_2 indices are differentially sensitive to the absorption by dust (Galactic or internal), and thus could be used to measure the amount of this absorption (this is done for some low-galactic-latitude objects in Burstein et al. 1987). In the present case, we only have selected high-latitude objects and the Galactic absorption is presumably small in front of them. Further discussion on this point would be out of the scope of the present paper, since it does not a priori interfere with the effect of the non-homology.

3.2. The Fundamental-Plane equation including the stellar-population effect

The analysis of the correlation between the residuals R to the FP and the stellar-population indicator defines the coefficient u:

$$R = uP. \tag{11}$$

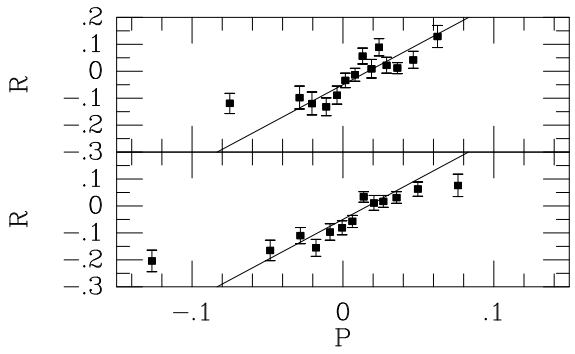

Fig. 2. The residuals from the Fundamental Plane (R) vs. the stellar-population indicator (P), with regression line (u = 3.0) superposed. Upper panel: bona fide ellipticals. Lower panel: whole sample. The data are assembled in bins of 40 galaxies. The error bars correspond to the 1σ error on the mean value of R for the considered bin, i.e., rms$/\sqrt{39}$

On the subsample of elliptical galaxies, we determine u = 2.6 $\pm$ 0.9, and for the whole sample u = 3.1 $\pm$ 0.9. We then adopt:

$$u = 3.0 \pm 0.9, \quad (12)$$

a value close to the coefficient fitted in PS96 for the $B-V$ color. The distribution of the observed residuals R as a function of P is shown in Fig. 2.

In order to take into account the population effect, we modify Eq.(8) and we define a new residual R' by:

$$R' = 2\log(\sigma_0) + 0.2(1+2\beta')M_B + 0.2\mu_e - uP + \eta'. \quad (13)$$

As explained in PS96, u was not directly derived by a fit to Eq. (8), because of the strong internal correlation between P and M_B.

With u determined, we have fitted Eq. (8) again, and we report the results in Table 1. The two solutions, with and without the stellar-population term, will be used to study the effect of the non-homology of the spatial structure. We will not consider, at this point, the inclusion of the rotational support since: (i) it is a secondary effect compared to that of the stellar population and, (ii) this would dramatically reduce the size of the sample owing to the limited availability of the rotational velocities.

4. Effect of the non-homology

Prior to searching the residuals R and R' for correlations with the Sérsic exponent, we will look for monovariate correlations involving this parameter and any one of the fundamental parameters.

4.1. Correlations between r_e, M_B and n

The Sérsic exponent has been found to correlate with the radius by CCO93. We present this diagram in Fig. 3. The Sérsic exponent seems to saturate for large galaxies ($\log(r_e[\mathrm{kpc}]) > 0.8$) to a value of ≈ 4 but depends strongly on the size for the smaller galaxies: $n = \kappa_1 + \kappa_2 \log(r_e)$. In Table 3 we summarize the coefficients κ_1 and κ_2 we fitted on different sets of data drawn from the literature, and we display these relations in Fig. 4.

CCO93 have determined the Sérsic exponent along both major and minor axes and along the equivalent axis, they give the relation: $\log(n_{\mathrm{maj}}) = 0.28 + 0.52\log(r_e)$ (for the major-axis n) actually much steeper than the relation derived from our measurements. This relation is confirmed on their sample enlarged by the Fornax galaxies measured with the same method by D'Onofrio et al. (1994), and, as the values reported in Table 3 show, despite the fact that the relation involving n measured along the equivalent axis is less steep, the discrepancy with our measurements remains (note that we rejected the data with $n > 10$ from the fits provided in Table 3). As already discussed, the Sérsic exponent determined by CCO93 is essentially sensitive to the shape of the photometric profile in the outer region of the galaxies, while our growth curve fit is rather sensitive to the inner part. This probably explain the differences, and we note that the difference between n_{maj} and n_{min} contains information about the detailed structure of galaxies that could be considered for a refined description of the effects of spatial non-homology.

Lauberts & Valentjin (1989: ESO-LV) fitted the photometric profiles obtained from the photographic ESO-B Schmidt survey to a Sérsic law. The corresponding values, for early-type galaxies ($t \leq -2$), are represented in Fig. 4 (we restricted the sample to the radial velocity range: $1000 < V[\mathrm{kms}^{-1}] < 10000$).

It is remarkable that despite the diversity of methods and photometric material, the three sets of data concerned by luminous ellipticals (i.e., non-diffuse) give consistent results.

Schombert (1986, 1987) gives a set of template equivalent photometric profiles for different absolute magnitude computed from photometric profiles of 342 galaxies. We have fitted these templates to Sérsic profiles and we report in Table 3 and Fig. 4 the resulting n vs. $\log(r_e)$ relation. The Sérsic exponents are smaller than those from the three previous samples, but the same trend is still present.

Davies et al. (1988) and Young & Currie (1995) fitted the equivalent photometric profiles for, respectively, Virgo and Fornax diffuse ellipticals, both from photographic material. These two studies give compatible results, but with exponents n about half those found for normal ellipticals of the same r_e.

Because of the correlation between radius and absolute magnitude (see, e.g., Djorgovski & Kormendy 1989), this implies a correlation with B_T. This correlation is shown in Fig. 5.

The n vs. M_B correlation is characterized by two regimes: (1) the low-luminosity galaxies ($M_B < -20$) display an increase of n with the luminosity, reaching the de Vaucouleurs value of n = 4 for $M_B = -20$; and, (2) the luminous galaxies show a constant mean $n \simeq 4$. This is probably an important feature to be accounted for by models of galaxy formation.

We present in Table 3 and Fig. 6 the fit of the n vs M_B relations for the literature samples: $n = \kappa_3 + \kappa_4 M_B$. Except Schombert (1987), the other data sets agree well. In particular, the two samples of diffuse ellipticals lie in the continuity of the samples of normal (and giant) ellipticals.

Table 3. Sérsic exponent vs. $\log(r_e)$ relation

Sample[1]	$N^{(2)}$	$\log(r_e)^{(3)}$	κ_1	κ_2	$N^{(2)}$	$M_B^{(4)}$	κ_3	κ_4
Literature samples								
CCO93 (major)	48	-0.2 ; 1.3	1.93	3.65	46	-15.8;-22.4	-11.8	-0.80
CCO93 (equiv.)	57	-0.4 ; 1.3	2.48	3.09	54	-15.8;-22.4	-9.6	-0.70
CCO93 (minor)	56	-0.4 ; 1.3	3.01	3.00	63	-15.8;-22.4	-11.9	-0.85
ESO-LV	699	-0.4 ; 1.3	2.59	0.93	699	-15.4;-22.7	-2.9	-0.30
Schombert	7	0.1 ; 1.4	0.91	3.07	7	-16.6;-22.1	-11.5	-0.73
Davies+88	187	-0.8 ; 0.8	1.14	0.76	187	-11.4;-16.9	1.5	0.03
Y&C95	84	-0.8 ; 0.7	0.92	0.97	85	-13.0;-16.2	-3.5	-0.31
Present sample								
Ellipticals	291	-0.4 ; 1.4	2.94	1.45	294	-16.0;-22.9	-3.8	-0.38
Whole sample	525	-0.9 ; 1.5	3.00	1.27	525	-14.4;-22.9	-2.6	-0.31
Ellipticals	212	-0.4 ; 0.8	2.68	2.19	103	-16.0;-20.0	-7.9	-0.59
Whole sample	418	-0.9 ; 0.8	2.90	1.63	255	-14.4;-20.0	-3.7	-0.38
Ellipticals	82	0.8 ; 1.4	4.24	0.01	191	-20.0;-22.9	2.5	-0.08
Whole sample	107	0.8 ; 1.5	3.63	0.49	270	-20.0;-22.9	2.4	-0.08

Note: (1) Davies+88 = Davies et al. (1988); Y&C95 = Young & Currie (1995). (2) Size of the sample. (3) Range in $\log(r_e$[kpc]). (4) Range in M_B.

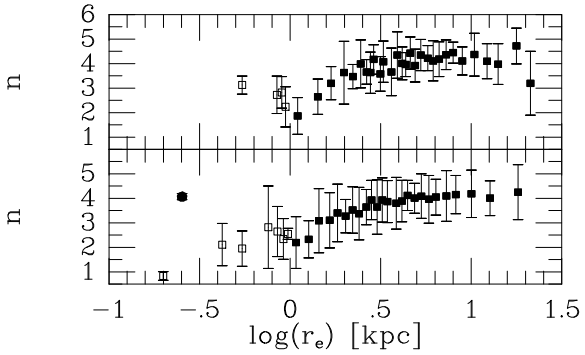

Fig. 3. Sérsic index (n) vs. $\log(r_e)$. Upper panel: bona fide ellipticals. *filled squares*: bins of 10 galaxies; *open square*: bins of 4 galaxies. Lower panel: whole sample. *filled squares*: bins of 20 galaxies; *open squares*: bins of 10 galaxies; *filled circle*: compact elliptical galaxies (3 objects). The error bars are the rms within each bin

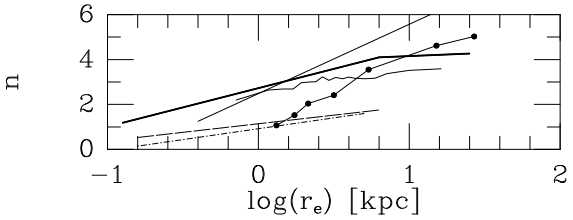

Fig. 4. Sérsic index (n) vs. $\log(r_e)$ for different samples. Thick line: Present sample. Thin line: CCO93 Broken line: ESO-LV (this line connects the centers of bins of 40 galaxies). Dots connected with a line: Schombert's (1987) templates. Dashed line: Davies et al. (1988); Dot-dashed line: Young & Currie (1995)

Since there exists a correlation between n and M_B, we can anticipate that the non-homology may contribute to the tilt of the FP.

4.2. Correlation between the FP residuals and n

We also searched for other possible correlations between n and parameters already known to enter the scaling relations. We do not find any correlation between n and the rotational support as it is formulated in PS94, but we found a trend of n with P, in the sense of the bluest (or Mg_2-weakest; i.e., lowest-P) galaxies exhibiting a lower n. We believe that this effect is a consequence of both parameters beeing strongly correlated with the luminosity.

However, in order to ensure that we are not overlooking a possible coupling, we will study both relations of n with R and R'. These relations are presented in Fig. 7. The general trend does not appear affected by the P-effect, but for galaxies with $n < 3$, the effect is significant. This concerns only the tail of this distribution while the P vs. R and n vs. R correlations are strongly constrained by the bulk of the distribution, and this confirms the looseness of the coupling. The non-homology effect is evidenced from the R' vs. n relation:

$$R' = 0.04(n - 4.6) \tag{14}$$

4.3. The tilt of the Fundamental Plane

Finally, we can investigate and summarize the different contributions to the tilt of the FP. Including the effects of stellar population, rotational support and non-homology, the FP equation can be generalized as follows:

$$R'' = 2\log(\sigma_0) + 0.2(1 + 2\beta'')M_B + 0.2\mu_e$$
$$+\delta\log(1 + 0.81(V_{\max}/\sigma_0)^2) - uP - vn + \eta''. \tag{15}$$

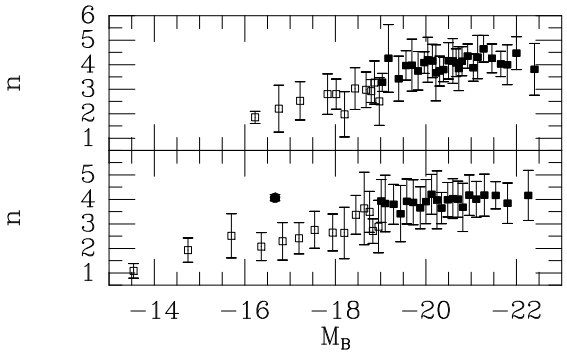

Fig. 5. Sérsic index (n) vs. Absolute B-magnitude (M_B). Upper panel: Bona fide ellipticals. *filled squares*: bins of 10 galaxies; *open square*: bins of 4 galaxies. Lower panel: Whole sample. *filled squares*: bins of 20 galaxies; *open squares*: bins of 10 galaxies. *filled circle*: Compact elliptical galaxies (3 objects). The error bars are the rms within each bin

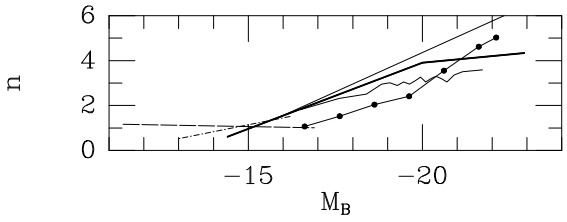

Fig. 6. Sérsic index (n) vs. M_B for different samples. Thick line: Present sample. Thin line: CCO93 Broken line: ESO-LV (this line connects the centers of bins of 40 galaxies). Dots connected with a line: Schombert's (1987) templates. Dashed line: Davies et al. (1988); Dot-dashed line: Young & Currie (1995)

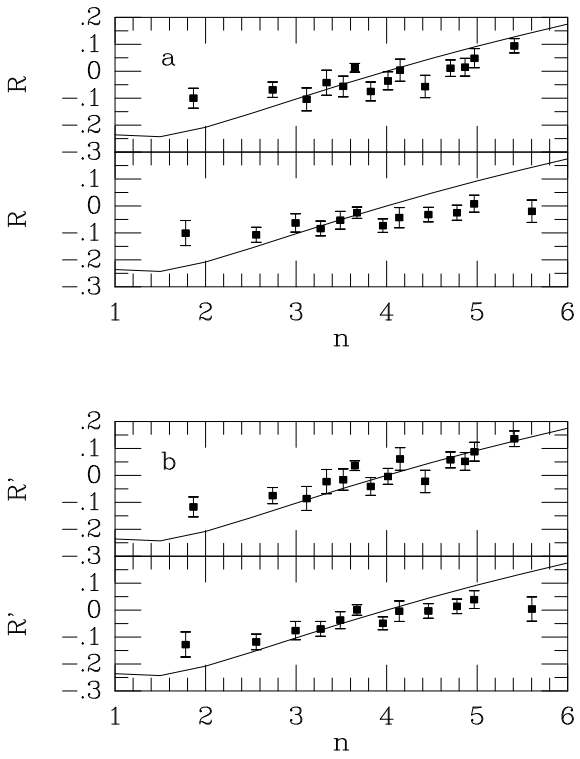

Fig. 7a and b. Residuals from the Fundamental Plane vs. Sérsic index n. **a** Residuals from the classical FP, (R), **b** Residuals corrected for the stellar-population effect, (R'). Upper panels: Bona fide ellipticals. Lower panels: Whole sample. The data are assembled in bins of 40 galaxies. The error bars are the 1σ error on the mean value of n for the considered bin, i.e., rms$/\sqrt{39}$. The overimposed line represents the variations of the dynamical factor: l_S

The actual value of the rotational support is taken from PS94, where we derived $\delta \approx 1$.

Using the values of u, δ and v constrained by Eqs. (11), (14) and (15), we report in Table 1 the fitted values of β''.

Including all identified contributions, the residual tilt vanishes within the errors.

The contribution of the spatial non-homology to the tilt of the FP is approximately half the one found by Hjorth & Madsen (1995). The detailed reasons for this disagreement are difficult to localise, since they use a different parametrization of the shape of the photometric profiles (i.e. the departure from $r^{1/4}$ law given by Burkert, 1993). However, the very small size of their comparison sample (22 galaxies) could probably be an explanation and we nevertheless note that we at least agree on the sign of the effect.

5. Expected effect of the non-homology

The non-homology enters the global scaling relation through the term l_S of Eq. (6). Thus, in the present framework, l_S is a function of the Sérsic exponent n which can be theoretically computed. Actually, deprojecting the Sérsic density profile, and considering isotropic spherical galaxies with constant $\mathscr{M}/L$ throughout, $l_S = S_D^{-1}$ is computed in Appendix B (Table 4 and Fig. 9).

As presented in Appendix B, l_S is in turn splitted into two components. The first, S_s, reflects the scaling of the gravitational energy by the effective radius (Eq. B8). The second, S_K, reflects the scaling of the kinetic energy by the central velocity dispersion (Eq. B10). Thus, the first effect is directly observed while the second is only its predicted consequence (and derived from an isotropic model, in the present case).

In principle, the kinematical effect of S_K could be observed by parametrizing the shape of the velocity-dispersion profile: this question will be addressed in a subsequent paper.

In Fig. 7, we have superposed to the observed R vs. n relation the curves of l_S and that of the spatial structure term alone (S_s), shifted in order to match the data: the agreement is very good.

Even if we ignore the galaxies with $n < 3$, which are, on average, affected by an important stellar-population effect, the fit is well within the measurement errors and the uncertainties attached to the adopted hypotheses on S_D (these are the isotropy and mostly the choice of the smoothing radius for defining σ_0).

6. Discussion and conclusions

6.1. The scaling relations for galaxies

We are now able to draw a detailed picture of the scaling relations for elliptical galaxies.

The scaling of the mass of the stars by the light can be characterized by a stellar-population indicator. In the present paper, we have defined the latter as a combination P of the broad-band colors and Mg_2.

The kinetic energy is almost a linear function of the squared central velocity dispersion. In the detail it has to be corrected for the rotational support.

The gravitational energy is constrained by the existence of a scaling radius, here r_e, and we have shown here that the shape of the radial distribution of the light introduces an additional term in this scaling relation.

Summing up all the observed scaling relations suggests that the $\mathscr{M}_*/\mathscr{M}$ ratio is constant for all early-type galaxies, in other words, that the proportion of dark matter (DM) is the same, in the central region probed by our kinematical data. This is at variance with other interpretations of the tilt of the FP, which require an increasing fraction of DM with mass (Renzini & Ciotti, 1993).

The scaling relations of early-type galaxies should be discussed in the frame of models for their formation and evolution. The scaling of the mass of the stars by their light probes the age distribution of the stellar population when looking back in time (Franx & van Dokkum 1996).

6.2. The compact and diffuse elliptical galaxies

The trends of the stellar population indicator P and the Sérsic exponent n with M_B and $\log(r_e)$ (Figs. 1, 3 and 5) call for a specific discussion. Two points may be noted:

- As a function of both M_B and $\log(r_e)$, the slope for faint galaxies is steeper than for bright ones.
- The compact elliptical galaxies depart from the general relations, being more metal-rich (or older) and having a larger Sérsic exponent ($n \approx 4$).

Actually, an alternative interpretation of these diagrams can be made: they could reflect the fact that the compact ellipticals are in the continuity of the bright galaxies, while the diffuse and dwarf spheroidals form a different sequence. This meets the classical interpretation of the distribution of galaxies in the $M_B - \mu_e$ diagram (Kormendy 1985; Nieto & Prugniel 1987; Binggeli 1994).

A preliminary investigation of the distributions of n and P in the $M_B - \mu_e$ plane (Maubon 1996) strengthens this idea. In the $P - M_B - \mu_e$ and $n - M_B - \mu_e$ spaces, galaxies seem to be distributed in planes corresponding to almost constant P and n along a line connecting bright ellipticals to compacts, and with decreasing P and n toward the diffuse and dwarf spheroidal galaxies. This confirms previous indications about the continuity between the two sequences of galaxies in terms of stellar population (Prugniel et al. 1992) and internal structure (Prugniel 1994).

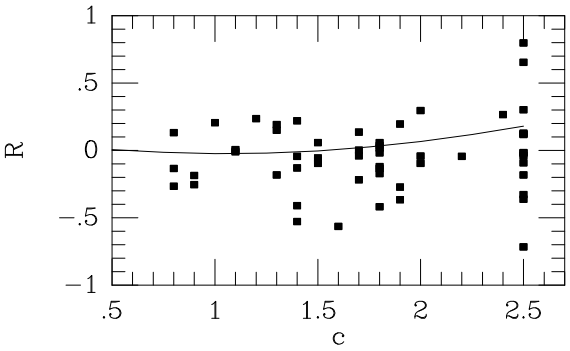

Fig. 8. Residuals from the Fundamental Plane vs. concentration index for the galactic globular clusters. The accumulation of points at $c = 2.5$ corresponds to the post core-collapse clusters. The curve is the expected effect of the non-homology in the density profiles for isotropic systems

6.3. The Fundamental Plane of globular clusters

The Galactic globular clusters are also known to lie on a FP (Nieto et al. 1990). This plane is tilted in a very similar way as that of early-type galaxies: the various determinations of β span the range $0.12 < \beta_{\rm GC} < 0.43$ (Schaeffer et al. 1993; Djorgovski 1995; PS96). However, unlike the case of early-type galaxies, this tilt is unaffected by the stellar-population effect (i.e., the population of the globular clusters do not depend on their luminosity). Djorgovski (1995) suggested that the tilt could result from the spatial non-homology. Using the same data as in PS96 and the concentration index c from Trager et al. (1993), we present in Fig. 8 the residuals from the FP vs. c for 57 clusters: no correlation is apparent. We have calculated (and superposed to the data) the $l_S = D_D^{-1}$ for a family of King profiles scaled by the central velocity dispersion; this calculation is qualitatively in agreement with the results of Bender et al. (1992) in their Appendix A. The range of l_S is small compared with the scatter in the observed residuals, and this supports the idea that the non-homology of the GCs does not contribute significantly to the tilt of their FP. This tilt thus remains unexplained, but we note that its value is also quite poorly determined: $\beta_{\rm GC} = 0.12 \pm 0.07$ in PS96.

6.4. Conclusion

We confirm the existence of relations between the shape of the luminosity profile, as parametrized by the Sérsic exponent, and the effective radius or the absolute magnitude and give indications for a saturation of this index for the bright ($M_B < -20$) or large ($r_e > 6.3$ kpc) galaxies at a value compatible with the de Vaucouleurs law ($n = 4$).

We have shown that the residuals from the FP correlate with the Sérsic exponent and that this effect of the structural non-homology in early-type galaxies is in agreement with the theoretical expectation for isotropic models. While we did not quantify the effect of a possible anisotropy, this result at least implies that the non-homology of the light echoes the non-homology of the mass.

Combining the contributions of: (i) the stellar population effect (PS96), (ii) the rotational support (PS94) and, (iii) the non-homology of the structure, the tilt of the FP is fully accounted for.

Combining the velocity-dispersion profile to the shape of the luminosity profile could possibly be used for testing the dynamical status, and, e.g., it may help in putting constraints on the degree of radial-to-tangential anisotropy. Recent studies have dealt with a very detailed kinematical analysis based on accurate 3D mass modelling and extensive spectroscopy of a reduced sample of objects (e.g., Binney et al. 1990; van der Marel et al. 1990); a more superficial, but potentially more statistical, approach could be provided by the determination of a gross anisotropy index as a function of the Sérsic index, from only major-axis spectra, and for a large sample of galaxies.

Acknowledgements. We thank the telescope operators of the Observatoire de Haute-Provence for their continuous help in collecting the data. We are indebted to Mauro D'Onofrio and James Lequeux, for valuable discussions and comments. We have made use of the SIMBAD and LEDA databases operated, respectively, by the CDS (Observatoire de Strasbourg) and by the Observatoire de Lyon.

Appendix A: circular-aperture growth curves for a Sérsic profile

In this Appendix we derive the circular aperture growth curve for the Sérsic profile. We assume a circular galaxy.

The Sérsic profile of exponent n is written in flux units:

$$f(x,n) = A\exp(-bx^{1/n}), \tag{A1}$$

where $f(x,n)$ is the *reduced* surface brightness (in flux scale) at the reduced radius x ($x = 1$ at the effective radius). The constants A and b are determined below to set the length scale and the luminosity scale (total *reduced* flux = 1), they are connected to ζ and ξ of Eq. 7 by: $\zeta = 1.086b$ and $\xi = -2.5\log(A/r_e^2)$.

The flux through a circular aperture of reduced radius x is then:

$$F(x,n) = 2\pi\int_0^x rf(r,n)dr = 2\pi A\int_0^x exp(-br^{1/n})rdr. \tag{A2}$$

Using the scaling definitions, $F(1) = 1/2$ and $F(\infty) = 1$, allows to compute the two constants A and b. We have obtained a numerical solution:

$$b = 2n - \frac{1}{3} + 0.009876/n, \tag{A3a}$$

and:

$$A = \frac{b^{2n}}{2\pi n\Gamma(2n)}. \tag{A3b}$$

The precision on b is $\delta(b) = 0.001$.

Eq. (A2) can be transformed in:

$$F(x,n) = 1 - \gamma(2n, bx^{1/n})/\Gamma(2n), \tag{A4}$$

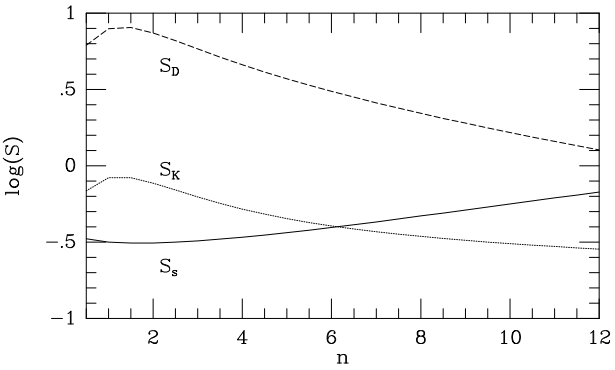

Fig. 9. Scaling factors of the Sérsic law

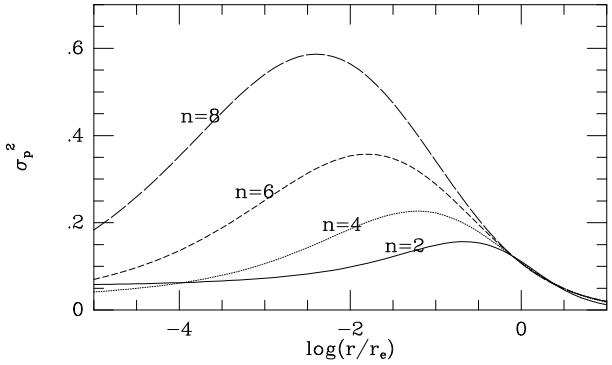

Fig. 10. Profile of the projected velocity dispersion. σ_p is in the units described in the text

where $\gamma(a,x) = \int_x^\infty t^{a-1}\exp(-t)dt$ is the incomplete γ function (see Abramowitz & Stegun 1964, p. 260). The FORTRAN code for computing $F(x,n)$ may be obtained from the authors.

Appendix B: deprojection and binding energy of the Sérsic profile

In this appendix we present the deprojection of the Sérsic profile and we derive the scaling relations for the gravitational and kinetic energies.

In the particular case of the de Vaucouleurs profile ($n = 4$), Young (1976: Y76) performed a numerical deprojection, and Mellier & Mathez (1987: MM87) presented a good approximation of this profile. Ciotti (1991) generalized these approaches and presented photometric and dynamical parameters for profiles of the type $r^{1/n}$, for n from 2 to 10. Here, we will give an adapted version of the deprojected density and its analytical approximation.

In the following, we adopt a mass-follow-light hypothesis, and thus deal with mass density only.

B.1. Deprojection of the density profile

Lets write the projected (ie. integrated along the line of sight) Sérsic density profile as:

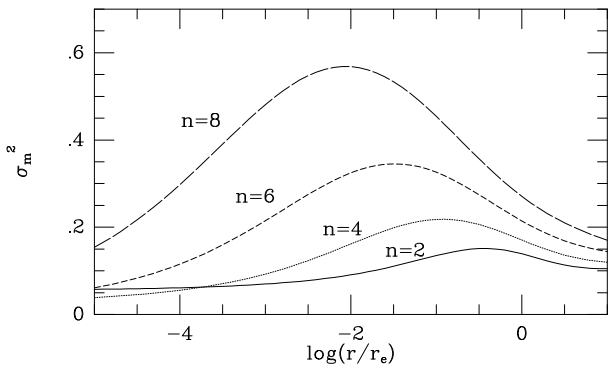

Fig. 11. The projected velocity dispersion averaged within a centered circular aperture of radius r; σ_m is in the units described in the text

Table 4. Scaling factors for Sérsic density profiles

Sérsic exponent	S_s	S_K	S_D
1	0.316	0.833	7.911
2	0.312	0.769	7.408
3	0.322	0.625	5.827
4	0.340	0.521	4.591
5	0.364	0.451	3.710
6	0.394	0.403	3.067
7	0.429	0.369	2.582
8	0.468	0.344	2.203
9	0.513	0.325	1.900
10	0.562	0.309	1.651

$$\rho_p(r) = \mathscr{M}\, A exp(-br^{1/n}), \tag{B1}$$

where $\rho_p(r)$ is the projected surface density at the *reduced* radius r, n the Sérsic exponent and $\mathscr{M}$ is the total mass. A and b are the constants determined in Appendix A.

The spatial density profile, $\rho(s)$, writes (Poveda et al. 1960):

$$\rho(s) = -\frac{1}{\pi}\int_s^\infty \frac{\rho'(r)}{\sqrt{r^2-s^2}}dr. \tag{B2}$$

Or, when replacing the derivative $\rho'(r)$ of $\rho(r)$:

$$\rho(s) = \mathscr{M}\frac{A\,b}{n\pi}\int_s^\infty \frac{r^{(1/n-1)}\exp(-br^{1/n})}{\sqrt{(r^2-s^2)}}dr, \tag{B3}$$

which we will transform in:

$$\rho(s) = \mathscr{M}\frac{A}{\pi}s^{-1}\exp(-b\,s^{1/n})\int_0^\infty \frac{exp(-u)}{\sqrt{(u/bs^{-1/n}+1)^{2n}-1}}du. \tag{B4}$$

Expanding Eq. B4 in a series of Γ functions for large values of s gives the asymptote:

$$\rho(s) = \mathscr{M}\,A\sqrt{\tfrac{b}{2\pi n}}s^{(1/2n-1)}\exp(b\,s^{-1/n})\times \left(1-\frac{2n-1}{8b}s^{-1/n}+...\right). \tag{B5}$$

Equation B5 generalizes the result for n = 4 given by Y76 and, truncated to its first term, is actually close to the true deprojected profile, except at the very center.

Following MM87, we will fit a simplified form for the density profile:

$$\rho(s) = \mathscr{M}\,A\,s^{-\alpha}\exp -bs^{1/n}, \tag{B6}$$

where α is the free parameter. For the de Vaucouleurs profile, MM87 found α = 0.855, a value close to the asymptotic $\alpha = 1 - 1/2n$ = 0.875.

We determine α by fitting the projected profile with the Sérsic profile. As MM87 have shown, α is not much dependent on the radial range used for the fit, and we use the results obtained by fitting in the range: $-1 < \log(r) < 2$.

Then, we fit $\alpha(n)$ by:

$$\alpha(n) = 1 - \frac{1.188}{2n} + \frac{0.22}{4n^2}. \tag{B7}$$

Note that for n = 4 this form gives: α = 0.855. Including, both effects of approximations on the spatial profile and on the use of Eq. A3, the error on α is: $\delta(\alpha)$ = 0.003.

B.2. Scaling relation for the gravitational energy

The gravitational energy is given by:

$$W(n) = -S_s(n)G\mathscr{M}^2/r_e, \tag{B8}$$

where G is the gravitational constant: if the lengths are given in kpc, the mass in solar mass and the velocity dispersion in km sec^{-1}, then $G = 4.30\times10^{-3}$. $S_s(n)$ is the scaling factor connecting the units of mass and length to the energy units (see, e.g., Y76).

$$S_s(n) = \frac{1}{2.\mathscr{M}^2}\int_0^\infty \left(\frac{\mathscr{M}(s)}{s}\right)^2 ds, \tag{B9}$$

where $\mathscr{M}(s)$ is the mass within the sphere of reduced radius s. Eq. B9 is numerically integrated, for n = 4 we find $S_s(4)$ = 0.340 while Y76 gives 0.336.

The variation of $S_s(n)$ is presented in Fig. 9 and in Table 4.

B.3. Scaling relation for the kinetic energy

As usual in FP analyses, we use the observed central velocity dispersion, σ_0, as the scaling parameter for the kinetic energy T:

$$T(n) = \frac{3}{2}\mathscr{M} < \sigma^2 >= S_K(n)\frac{3}{2}\mathscr{M}\sigma_0^2, \tag{B10}$$

where $< \sigma^2 >$ is the density weighted averaged one-dimensional velocity dispersion and $S_K(n)$ the kinematical scaling factor.

In order to determine σ_0 (affected by the spatial resolution of the observations) we compute the velocity dispersion projected along the line of sight, $\sigma(r)$, in the case of isotropic systems. The equations of stellar dynamics give the spatial one-dimensional velocity dispersion $\sigma_s(r)$ (Binney 1980):

$$\sigma_s(r)^2 = \frac{G}{\rho(r)} \int_r^\infty \rho(s).\mathscr{M}(s) s^{-2} ds. \qquad \text{(B11)}$$

The projected velocity dispersion is obtained by integrating Eq. B11 along the line of sight intercepting the center:

$$\sigma(r)^2 = \frac{2G}{\rho_p(r)} \int_r^\infty \frac{\sqrt{s^2 - r^2}}{s^2} \rho(s).\mathscr{M}(s) ds. \qquad \text{(B12)}$$

As shown by Binney (1980) for $n = 4$, and by Ciotti (1991), the central projected velocity dispersion is somewhat lower than its peak value. We note, however, that our central depression is much deeper, due to the fact that our calculations are given down to $\log(r/r_e) = -5$. This phenomenon, growingly marked for larger n, is illustrated in Fig. 10.

The reduced radius of the peak, varying from $r_{\rm peak}/r_e = 0.25$ for $n = 2$ down to 0.004 for $n = 8$, is much smaller than the spatial resolution of the observations, and consequently, $\sigma(0)$ does not reflect the value of σ_0 (the observed value). Fig. 11 shows an effect of the spatial resolution: at each r, $\sigma_{\rm m}$ is the luminosity-weighted average of σ within the centered aperture of radius r. The mean r_e for the galaxies of our sample is $< \log(r_e) >= 1.3$ with a rms dispersion of $\delta(\log(r_e)) = 0.3$. Thus for a typical spatial resolution of 2 arcsec for the observations, the radius used for the scaling lies in the range $-1.6 < \log(r/r_e) < -1.0$. For n between 2 and 6, this range imply an uncertainty of 20% on S_D.

We define σ_0 as the luminosity-weighted $\sigma(r)$ within $r_0 = 0.1 r_e$ (we note that Jørgensen et al. 1993 have found that this aperture is typical of the published measurements on nearby galaxies, although they argue that it is still too small to take into account all the kinetic energy; presumably, this is especially the case for rotating objects).

Finally, using the virial theorem with T and W from Eq. B8 and B10, we derive S_K:

$$S_K(n) = \frac{S_S(n)}{3} G \frac{\mathscr{M}}{\sigma_0^2 r_e}. \qquad \text{(B13)}$$

$S_K(n)$ is represented in Fig. 9 and Table 4.

Equation B13 may be used to determine the mass of a galaxy, knowing its observed r_e and σ_0:

$$\mathscr{M} = \frac{3\, S_K(n)}{S_s(n)} \frac{1}{G} r_e \sigma_0^2. \qquad \text{(B14)}$$

The factor:

$$S_D(n) = \frac{3\, S_K(n)}{S_s(n)} \qquad \text{(B15)}$$

is the dynamical scaling factor. As already noted by Michard (1980), $S_D(4) = 4.6$ should replace the factor 9 in the classical Poveda formula. The values of $S_D(n)$ are presented in Fig. 9 and Table 4.

References

Abramowitz, M., Stegun, I.E. 1964, Handbook of Mathematical Functions

Binggeli, B. 1994, in Meylan, G., Prugniel, Ph. (Eds.), Dwarf Galaxies, ESO Proceeding 49, 13

Binney, J.J. 1980, MNRAS 190, 873

Binney, J.J., Davies, R.L, Illingworth, G.D. 1990, ApJ 361, 78

Bender, R., Burstein, D., Faber, S.M. 1992, ApJ 399, 462

Bender, R., Saglia, R. P., Gerhard, O. E. 1994, MNRAS 269, 785

Burkert, A. 1993, A&A 278, 23

Burstein, D., Heiles, C. 1982, AJ 87, 1165

Burstein, D., Davies, R.L., Dressler, A., et al. 1987, ApJS 64, 601

Buta, R., Corwin, H.G., de Vaucouleurs, G., de Vaucouleurs, A., Longo, G. 1995, AJ 109, 517

Caon, N., Capaccioli, M., D'Onofrio, M. 1993, MNRAS 265, 1013 (CCO93)

Ciotti, L. 1991, A&A 249, 91

Davies, R. L., Burstein, D., Dressler, A., et al. 1987, ApJS 64, 581

Davies, J.I., Phillipps, S., Cawson, M.G.M., Disney, M.J., Kibblewhite, E.J. 1988, MNRAS 232, 239

de Vaucouleurs, G., de Vaucouleurs, A., Corwin, H.G., Jr., Buta, R.J., Paturel, G.,et al. 1991, Third Reference catalogue of Bright Galaxies (Springer, New York) (RC3)

Djorgovski, S. 1995, ApJ 438, L29

Djorgovski, S., Davis, M. 1987, ApJ 313, 59

Djorgovski, S., Kormendy, J. 1989, ARA&A 27, 235

D'Onofrio, M., Capaccioli, M., Caon, N. 1994, MNRAS 271, 523

D'Onofrio, M., Prugniel, Ph. 1996, in Persic, M., Salucci, P. (Eds.) Dark and visible matter in galaxies, ASPCS, in press

D'Onofrio, M., Longo, G., Capaccioli, M. 1995, in Buzzoni, A., Renzini, A., Serrano, G. (Eds.) Fresh views of elliptical galaxies, ASPCS 86, 143

Dressler, A., Lynden-Bell, D., Burstein, D., et al. 1987, ApJ 313, 42

Dressler, A., Faber, S.M., Burstein, D. 1991, ApJ 368, 54

Faber, S.M., Burstein, D. 1988, in Rubin, V.C., Coyne, G.V. (Eds.) Large-Scale Motions in the Universe (Princeton Univ. Press, Princeton), p. 115

Franx, M., van Dokkum, P. 1996 in Bender, R., Davies, R.L. (Eds.) New light on galaxtic evolution (Kluwer, Dordrecht), in press

Gregg, M.D. 1992, ApJ 384, 43

Guzmán, R., Lucey, J.R. 1993, MNRAS 263, L47

Hamabe, M., Kormendy, J. 1987, in de Zeeuw, T. (Ed.), Structure and dynamics of elliptical galaxies (Reidel, Dordrecht), p. 379

Hjorth, J., Madsen, J. 1995, ApJ 445, 55

Jørgensen, I., Franx, M., Kjaergaard, P. 1993, ApJ 411, 34

Jørgensen, I., Franx, M., Kjaergaard, P. 1995, MNRAS 276, 1341

Kormendy 1985, ApJ 295, 73

Lauberts, A., Valentjin, E. 1989, The Surface Photometry Catalogue of the ESO-Uppsala Galaxies (ESO, Garching) (ESO-LV)

Maubon, G. 1996, Observatoire de Lyon: Rapport de stage de DEA

Mellier, Y., Mathez, G. 1987, A&A 175, 1 (MM87)

Michard, R. 1980, A&A 91, 122

Nieto, J.-L., Prugniel, Ph. 1987, A&A 186, 30

Nieto, J.-L., Bender, R., Davoust, E., Prugniel, Ph. 1990, A&A 230, L17

Persic, M., Salucci, P. 1990, MNRAS 245, 577
Poveda, A., Iturriaga, R., Orozco, I. 1960, Bol. Obs. Tonantzintla y Tacubaya 20, 3
Prugniel, Ph., Bica, E., Alloin, D. 1992 in Longo, G., Capaccioli, M., Busarello, G. (Eds.) Morphological and physical classification of galaxies (Kluwer, Dordrecht), p. 261
Prugniel, Ph. 1994, in Meylan, G., Prugniel, Ph. (Eds.), Dwarf Galaxies, (ESO Proceeding, Garching) 49, 171
Prugniel, Ph., Simien, F. 1994, A&A 281, L1 (PS94)
Prugniel, Ph., Simien, F. 1995, in Buzzoni, A., Renzini, A., Serrano, G. (Eds.) Fresh views of elliptical galaxies, ASPCS 86, 151
Prugniel, Ph., Simien, F. 1996, A&A 309, 749 (PS96)
Renzini, A., Ciotti, L. 1993, ApJ 416, L49
Saglia, R.P., Bender, R., Dressler, A. 1993, A&A 279, 75
Schombert, J.M. 1986, ApJS 60, 603
Schombert, J.M. 1987, ApJS 64, 643
Schaeffer, R., Maurogordato, S., Cappi, A., Bernardeau, F. 1993, MNRAS 263, L21
Sérsic, J.-L. 1968, Atlas de galaxias australes, Observatorio Astronómico de Córdoba
Trager, S. C., Djorgovski, S., King, I. R. 1993, in Djorgovski, S., Meylan, G. (Eds.) Structure and dynamics of globular clusters, ASPCS 50, 337
van Albada, T.S., Bertin, G., Stiavelli, M. 1995, MNRAS 276, 1255
van den Bergh, S. 1989, A&AR 1, 111
van der Marel, R.P., Binney, J.J., Davies, R.L. 1990, MNRAS 245, 582
Young, P.J. 1976, AJ 81, 807 (Y76)
Young, C.K., Currie, M.J. 1995, MNRAS 273, 1141
Zepf, S.E., Silk, J. 1996, ApJ, in press

This article was processed by the author using Springer-Verlag LaTeX A&A style file *L-AA* version 3.